

# Tunable collective behavior in active cytoskeletal assemblies

Simon L. Freedman, Shiladitya Banerjee, Glen M. Hocky, Aaron R. Dinner

## Abstract

Cells can modulate the mechanical properties of the actin cytoskeleton in remarkable ways to maintain structural integrity, move and divide. This behavior is achieved through crosslinking proteins and bundling agents that dynamically control cellular structure, as well as active motors that generate active stresses and regulate intracellular transport. *In vitro* model systems using a small subset of purified proteins have revealed the minimal components necessary to confer this wide range of mechanical behaviors. Here, we take the same approach using agent-based computational modeling, and investigate the collective dynamics of disordered cytoskeletal assemblies, consisting of semi-flexible filaments, dynamic crosslinkers, and molecular motors. By tuning the properties of individual cytoskeletal elements, such as filament length, crosslinker stiffness, or motor kinetics, we explore the collective phases of actomyosin networks across dynamic regimes inaccessible to experiments. Our work elucidates the diverse pathways for cytoskeletal contractility, polarity organization, and molecular transport, and provides testable predictions for future experiments on reconstituted cytoskeletal assemblies.

## 1 Introduction

The actin cytoskeleton serves as a dynamic scaffold that allows eukaryotic cells to actively change shape, move, and adapt to their micro-environment. Although the cellular cytoskeleton constitutes a complex network of protein-protein interactions, *in vitro* model systems have revealed the minimal set of components required to exhibit a wide range of active mechanical behaviors including contractility and polarity organization [1–3]. In this work, we investigate the range of collective behaviors accessible to a minimal system consisting of cytoskeletal filaments, crosslinking proteins, and active molecular motors. While previous studies have shed light on the mechanisms of contractility and self-organization in minimal cytoskeletal systems [1, 3–7], a necessary limitation is the difficulty to precisely control physical properties of their protein constituents. Thus, it is poorly understood how variations in filament stiffness, length, crosslinker geometry, and affinity control emergent properties of cytoskeletal assemblies. Here, we present an agent-based model of the actin cytoskeleton, using non-equilibrium molecular dynamics, that can efficiently explore the collective phases of crosslinked actomyosin networks. Our agent-based model is ideal for elucidating the relationship between protein-protein interactions at the microscale and the collective mechanical behavior of the assembly. Furthermore, our dynamic simulations enable us to learn how active networks sample through dynamic states, and how intermediate mesoscopic structures may tune network functionality at cellular scales.

Actomyosin contractility has been extensively studied in the context of muscle cells, where actin filaments are arranged in a sarcomeric fashion, enabling myosin minifilaments to translocate two anti-parallel actin filaments and yield active muscle contraction [8]. However, the cytoskeleton of nonmuscle cells, exhibits no inherent ordering of actin or myosin filaments, yet F-actin buckling has been shown to coordinate long-range contractile behavior [1, 9, 10]. Recent *in vitro* studies using reconstituted networks of actin and myosin, have revealed how changing myosin concentration and F-actin properties effect the ability of a disordered networks to contract and form static structures [1, 2, 11]. For instance, at low motor density, the actin network behaves as non contractile, resulting in long-distance translocation of myosin along actin tracks [12]. Above a critical density, myosin motors cooperatively contract the actin network. Additionally, it has been shown that actin binding proteins (crosslinkers) such as filamin, scruin, and  $\alpha$ -actinin, can profoundly affect long-range force propagation as well as the mechanical stability of actin bundles and network [1, 2, 10, 13]. While these experiments are beginning to suggest the phase space of collective behavior in active networks, agent based simulations can explore in a controlled fashion how myosin density, actin bundle rigidity, and crosslinker density are able to modulate structure formation and force generation within the cell cytoskeleton.

To probe the microscopic origin of these complex collective processes, we propose an agent-based simulation model, motivated both by *in vitro* experiments as well as *in vivo* mechanical studies on actin and myosin [14, 15]. Our model also incorporates essential features from previous modeling work. Some of these models were designed to understand rheological properties of crosslinked actin networks [16–19], some have investigated the collective motion of motors on cytoskeletal tracks [20–22], and others have shown how disordered assemblies of filaments and motors collectively form asters [23] or induce network-level contraction [5–7, 24]. We use the worm-like chain model for an actin filament with both bending and stretching energies [20] and initialize networks with crosslinkers at filament intersections to form well connected networks [17]. In contrast to references [5, 17], we simulate non-equilibrium dynamics, including thermal fluctuations, stochastic binding and unbinding kinetics of myosins and crosslinkers, and myosin translocation. Force propagation rules, binding kinetic equations, and motor precession will be similar to [20, 23] with minor differences in implementation.

We accurately bench-mark our simulations to reproduce well known experimental results for actin filament dynamics, as well as the collective behavior of crosslinked actin and myosin driven active networks. We quantitatively reproduce the experimentally measured spatio-temporal fluctuations of single actin filaments. For passive crosslinked networks we recover the well-established stress strain relationships measured for semiflexible polymer networks [13, 25–27]. For active networks, we reproduce the experimentally observed velocity distributions of actin filaments in an actomyosin motility assay. These results demonstrate that our simulations capture several key properties of cytoskeletal networks within a single agent-based model.

We then show that our simulations predict diverse collective dynamical behaviors in cytoskeletal assemblies, and that tuning properties of filaments, crosslinkers, and motors, effects this collective behavior. We find that crosslinker affinity modulates filament bundling and network coarsening in a biphasic manner. We further show that crosslinker stiffness can tune the strain stiffening response of actin networks in a simulated rheology experiment. We quantify motor-dependent contraction in active networks and predict how the concentration of motors controls actin polarity sorting. These results suggest actomyosin contractility emerges from a competition between bundling and polarity sorting. We characterize study how variations in actin filament length, motor density, and motor-filament binding can alter motor cooperativity to translocate actin filaments, which may have implications for optimizing the observed dy-

namics of polarity sorting and contractility. Collectively our work demonstrates how ensembles of randomly oriented actin filaments and crosslinkers can be rearranged by myosin motors to form tunable structures with distinct biophysical and mechanical functionalities.

## 2 Results

An essential mechanical function of actomyosin networks is their contractility, which coordinates a variety of cellular processes, including muscle contraction, cell motility and division. That these complex macroscopic mechanisms arise stochastically from simple microscopic interactions suggests the ability to engineer materials with controllable network topologies and dynamics. Recently, in-vitro experiments of reconstituted actomyosin networks have demonstrated this controllable architecture by varying motor density and crosslinker density and showing how they effect contractility [1, 2]. Our model shows a similar dependence of network contractility on motor density. Additionally, we demonstrate tunability between two modes of network organization: bundling, in which dynamic crosslinkers pin filaments into robust networks, and polarity sorting, in which motors organize filaments into structures of uniform polarity.

For computational efficiency we have chosen to coarse grain actin filaments, and crosslinker proteins at length scales relevant for network behavior. Actin filaments are modeled as polar worm-like chains (WLC) such that one end of the chain represents the barbed end of a filament and the other end represents its pointed end. Crosslinkers are modeled as Hookean springs such that both ends of the spring (heads) can bind and unbind from filaments. Experiments have shown that adding crosslinkers to assemblies of F-actin yields actin bundles [1, 2, 13] and that increasing crosslinker density can increase the length scale of contraction [1]. We show that varying the stiffness of these springs modulates the rheology of an assembly of crosslinkers and filaments, while varying the binding affinity effects the magnitude of actin bundling. We parameterized our model in  $2D$  similar to the nearly flat in vitro reconstitutions of actomyosin. This setup is sufficient to reproduce structures of biological interest, and allows us to simulate large systems for long times. Because we use a  $2D$  system to model a  $3D$  experiment, we exclude the steric interactions of filaments and crosslinkers, to allow for some of the freedom lost from the reduction in dimensionality.

### 2.1 Crosslinker turnover modulates bundling of filament networks

The rapid binding and unbinding of crosslinking proteins from actin filaments can reorganize initially disordered filament networks into thick bundled networks. This behavior is distinct from motor-driven contractility, because the overall network structure coarsens without any active force generation. Here we tune this bundling mechanism by changing the crosslinker-filament binding affinity.

To demonstrate this behavior, thirteen simulations were initialized with 500  $15\mu m$  worm-like-chain filaments scattered on a  $75\mu m \times 75\mu m$  simulation cell, and  $0.15\mu m$  crosslinkers are placed at filament-filament intersections as shown in Figure 1A. The assemblies are then evolved via Brownian dynamics for  $200s$ . Each simulation had a different dissociation rate for crosslinkers  $k_{off}^{cl}$  varying logarithmically between  $0 - 1800s^{-1}$ . The results are shown in Figure 2.

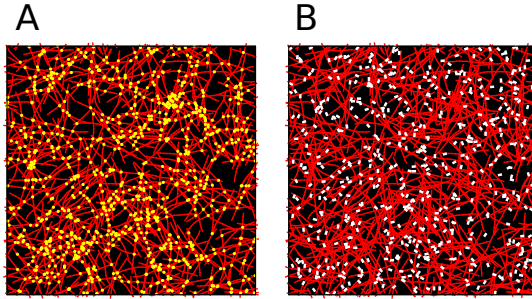


**Figure 1:** Initial configuration of actin filaments (red) for (A) assemblies which initially have crosslinkers (yellow, one third shown) placed at intersections and (B) assemblies with motors  $\rho_m = 0.1 \mu\text{m}^{-2}$  (white) scattered throughout.

The degree of bundling can be quantified by the radial distribution function of actin filaments,  $g(r) = P(r)/(2\pi r \delta r \rho)$  where  $P(r)$  is the probability that two beads on different filaments are separated by a distance  $r$ ,  $\delta r = 0.05 \mu\text{m}$  is the bin size and  $\rho = 500/(75 \mu\text{m})^2$  is the number density. As seen in Figure 2C-D, the relationship between  $k_{off}^{cl}$  and  $g(r)$  is non-monotonic. A low disassociation rate does not allow for significant restructuring from the initially random configuration, while a high disassociation rate will not yield long-lived stable structures. However, at intermediate values of  $k_{off}^{cl}$ , the filaments self-assemble into a stable, thickly bundled network.

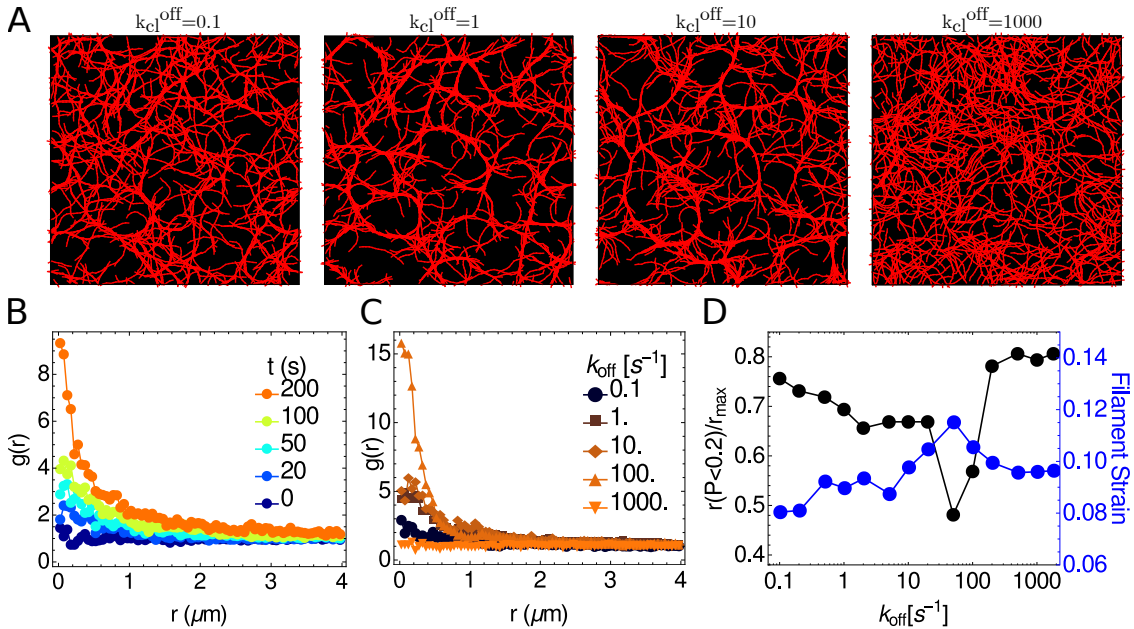


**Figure 2:** (A) Network configuration at  $t = 200\text{s}$  for varying disassociation constants of crosslinks (not shown). Filaments are shown in red. (B) Radial distribution function of beads on an actin filament for the  $k_{off} = 20 \text{ s}^{-1}$  at various times throughout the simulation. As the simulation proceeds, the higher peak at lower  $r$  values shows increase in bundle thickness. (C) Radial distribution function of actin filaments at  $t = 200\text{s}$  for varying  $k_{cl}^{off}$ . The curves show non-monotonic behavior, as both high and low  $k_{cl}^{off}$  have a shorter correlation length than curves with mid-range  $k_{cl}^{off}$ . (C) We measure this monotonicity by marking the distance at which 80% of the area under the curves in (B) are covered. Lower values mean longer decorrelation lengths, indicating a larger magnitude of bundling. We also show that the difference in filament strain across these simulations is minimal, less than 0.025, and shows no clear relationship with the radial distribution functions. Contrast this with contracting networks in Figure 6, where where filament strain ranges from 0 to 0.35 and correlates with network divergence.

## 2.2 Tunable elastic behavior of crosslinked filament networks

The mechanical properties of cross-linked F-actin networks are generally inferred using rheological measurements [13, 25–27]. In a typical rheology experiment, actin and crosslinker proteins are mixed to form a crosslinked mesh and then sheared in a rheometer by a prestress  $\sigma_0$ . The prestressed network is then subjected undergoes a sinusoidal differential stress of magnitude  $d\sigma \ll \sigma_0$ . By measuring the resulting strain, one can calculate the differential elastic modulus  $G(\sigma_0) = \frac{d\sigma}{d\gamma}$ . In experiments using a stiff crosslinker, such as scrulin, the dependance of the differential modulus on high prestress is  $G \propto \sigma_0^{3/2}$ , indicating that this shear stiffening is a direct result of the nonlinear force-extension relationship of actin [13, 27]. Experiments using more compliant crosslinkers, such as filamin, have found a softer stiffening response,  $G \propto \sigma_0$ , indicating that a significant amount of stress is mediated through the crosslinkers, and not the filaments [26].

These results suggest that the strain stiffening behavior of a crosslinked network can be tuned by varying the crosslinker stiffness. To test this possibility, the configuration of filaments shown in Figure 1 was reproduced with varying crosslinker stiffness  $k_{cl}$ . To inhibit network restructuring, the detachment rate of the crosslinkers was set to zero. An affine strain of  $\delta\gamma = 0.001$  was applied such that the horizontal position of every actin bead ( $x_a$ ) was shifted according to

$$x_a \rightarrow x_a + \delta\gamma \left( \frac{y_a}{Y} \right) \quad (1)$$

following the overdamped SLLOD equations of motion [28]. The periodic boundary was simultaneously shifted following the Lees-Edwards convention [29]. The mesh was then allowed to relax for  $t_{relax} = 0.001s$  before the next strain of  $\gamma$ . This protocol was continued for  $T_f = 0.5s$  allowing the total strain to reach a value:  $\gamma T_f / t_{relax} = 0.5$ . Increasing  $t_{relax}$  did not significantly change the simulation results as seen in Figure S2(a).

The elastic behavior of the network for each crosslinker stiffness was measured by calculating  $w$ , the strain energy density at each timestep

$$w(t) = \frac{1}{XY} \left( \sum_f U_f + \sum_{cl} U_{cl} \right) \quad (2)$$

where  $U_f$  is the mechanical energy of individual filaments (see Methods) and  $U_{cl}$  defines the potential energy of each cross link. By averaging over windows of size  $t_{relax}$ , we determine  $w(\gamma)$ . Figure 3 shows the results of these calculations for various values of crosslinker  $k_{cl}$ . By varying the ratio of filament to crosslinker stiffness, we were able to modulate the scaling exponent of the power law dependence of strain energy on the strain. For extremely low  $k_{cl}$ , the strain energy scaled linearly with strain,  $w \propto \gamma$ , indicating that the network showed no resistance to shear:  $G = \frac{d^2 w}{d\gamma^2} = 0$ . For high  $k_{cl}$ , we observe a neo-hookean strain stiffening behavior,  $w \rightarrow \gamma^4$  [30]. Thus, one can tune the behavior of these networks from being liquid-like, with  $w \propto \gamma$ , through the hookean elastic regime of  $w \propto \gamma^2$  as well as strain stiffening regimes of  $w \propto \gamma^3$  and  $w \propto \gamma^{3.5}$ , as previously reported in experiments [13, 26].

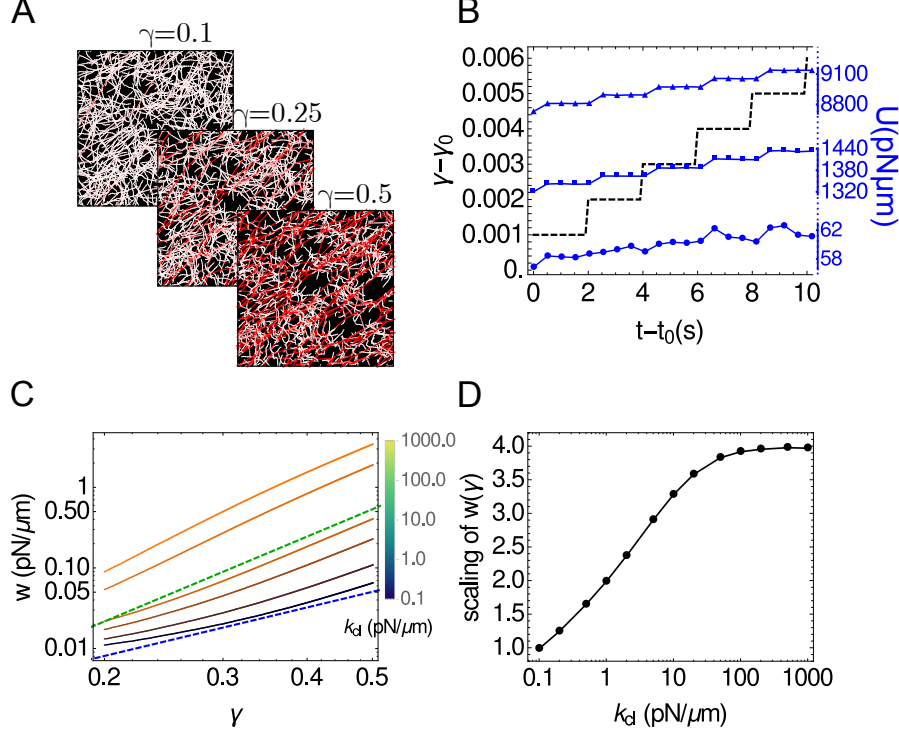


**Figure 3:** (A) Snapshots of a strained network ( $k_a = k_{cl} = 1000$ ) at  $t = 0.1s$ ,  $t = 0.25s$  and  $t = 0.5s$ . Color indicates stretching energy on each link, with white being the lowest and red being the highest. (B) The potential energy of the network as a function of time shown at different strains  $\gamma_0 = 0.1$  (circles)  $\gamma_0 = 0.25$  (squares) and  $\gamma_0 = 0.4$  (triangles) where  $t_0 = \gamma_0 \times 1s$ . Black dashed line shows the strain protocol. (C) Strain energy density ( $w = U/\text{area}$ ) for various values of crosslinker stiffness  $k_{cl}$ . Blue dashed line indicates expected behavior for a linearly elastic solid  $w \propto \gamma^2$  and green dashed line indicates strain stiffening behavior of  $w \propto \gamma^{3.5}$  as expected for semiflexible polymer networks [13, 27]. (D) Power law exponent of  $w(\gamma)$ , evaluated via least squares fit to  $\ln(\gamma)$  vs  $\ln(w)$ .

### 2.3 Cooperative sorting of filament polarity by molecular motors

Molecular motors are modeled as active crosslinkers such that a bound head precessively walks toward the barbed end of the filament with load dependent speed and kinetic (see Methods for details). This implementation allows for active filament sliding and filament buckling, as elucidated in Figure 4, both of which are instrumental for actomyosin contractility [1]. In large networks, motors can translocate across filaments, induce filament buckling, and also enhance network connectivity [2].

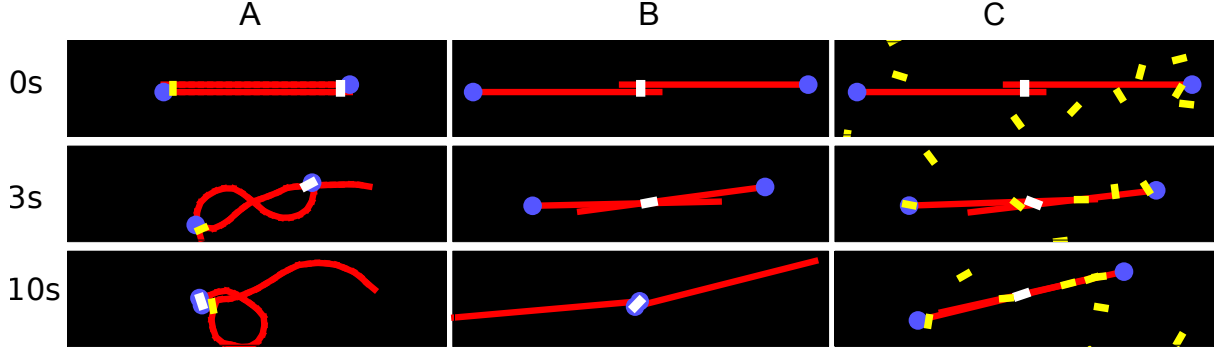


**Figure 4:** Time series of three antiparallel  $10\mu\text{m}$  filaments (red) interacting with a minimal set of motors (white) and crosslinkers (yellow) for 10s. Barbed ends of filaments are marked by a blue dot. (A) Filaments are semiflexible (21 bead-spring chain) and pinned on the left by a crosslinker, so the motor-filament interaction yields contraction via buckling. (B) Filaments are rigid (2-bead-spring chains) and unpinned, so motor-filament interaction yields unimpeded sliding of filaments. As a result, they transition from an initially extended state, to a contracted state at  $t = 3\text{s}$  and back to a fully extended polarity sorted state at  $t = 10\text{s}$ . (C) Filaments and motor are the same as (B) but with a population of crosslinkers near the filaments that arrests the filaments in a contracted state.

To isolate the role of active motors on assemblies of semiflexible filaments, the actin assembly in Figure 1 was generated without crosslinkers at filament intersections, but with  $0.5\mu\text{m}$  long motor minifilaments scattered uniformly throughout the simulation cell. In these simulations, the motor duty ratio was kept near unity to replicate the behavior of a myosin minifilament, while the density of motors was varied between different simulations. The results, shown in Figure 5, indicate that at higher motor densities, filaments are sorted by polarity, but are not clustered in space. Motors aggregated on the barbed ends of filaments and thereby brought the different barbed ends together to form asters. The magnitude of polarity sorting was measured by calculating the average distance of a bound motor from the barbed end of filament to which it was bound. As seen from Figure 5A-B, increasing motor density had the effect of decreasing this distance, indicating a larger magnitude of polarity sorting. It appears therefore that this form of polarity organization and restructuring is highly tunable.

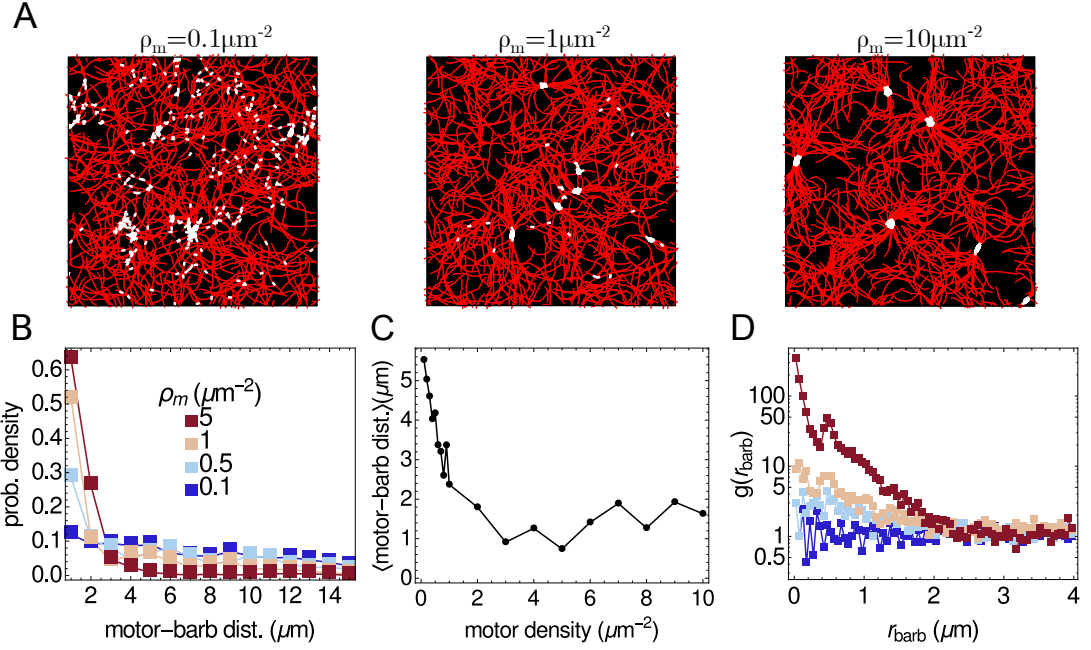


**Figure 5:** (A) Networks at their polarity sorted end configuration ( $t = 96\text{s}$ ). Filaments are shown in red, motors in white. A maximum of 1000 motors are shown in each case. (B) Probability density of the distance of an attached motor head from the barbed end of the filament to which it is attached for varying motor density at  $t = 96\text{s}$ . (C) The average distance of a motor head from the barbed end as a function of motor density. (D) Radial distribution function for barbed ends shows a strong dependence on motor density. For  $\rho_m = 5 \mu\text{m}^{-2}$ , a prominent secondary peak is also visible at the motor rest length  $l_m = 0.5 \mu\text{m}$ .

## 2.4 Contractility emerges from competition between bundling and polarity sorting

When both crosslinkers and motors are mixed with semiflexible filaments, the assemblies become contractile. To elucidate this behavior, actin filament assemblies were initialized (see Figure 1) with crosslinkers at their intersections with motors scattered uniformly throughout the cell. The motor density varied between simulations from  $0.1 - 10 \mu\text{m}^{-2}$ . The crosslinkers were kept sticky with a low duty ratio, while the motors were highly active with a high duty ratio. This ensured that connectivity of the network was almost exclusively controlled by crosslinkers while force generation was controlled by motors.

The results of these simulations and the final network configurations can be seen in Figure 6. The net contractility was measured by interpolating a velocity field from the displacement vectors of filament beads, and measuring the divergence of the velocity fields. A negative divergence indicates a net contractile behavior. As evident in Figure 6(B), higher motor density leads to larger contractility. Figure 6(D) shows that actin buckling, here measured as the change in the end to end distance  $\Delta s$  of an actin filament:

$$\Delta s = \left( 1 - \frac{|r_{15} - r_0|}{\sum_{i=1}^{15} |r_i - r_{i-1}|} \right) \quad (3)$$

correlates with contractility, suggesting that the primary mechanism driving contractility in these flexible networks is filament buckling, as observed in experiment [1].

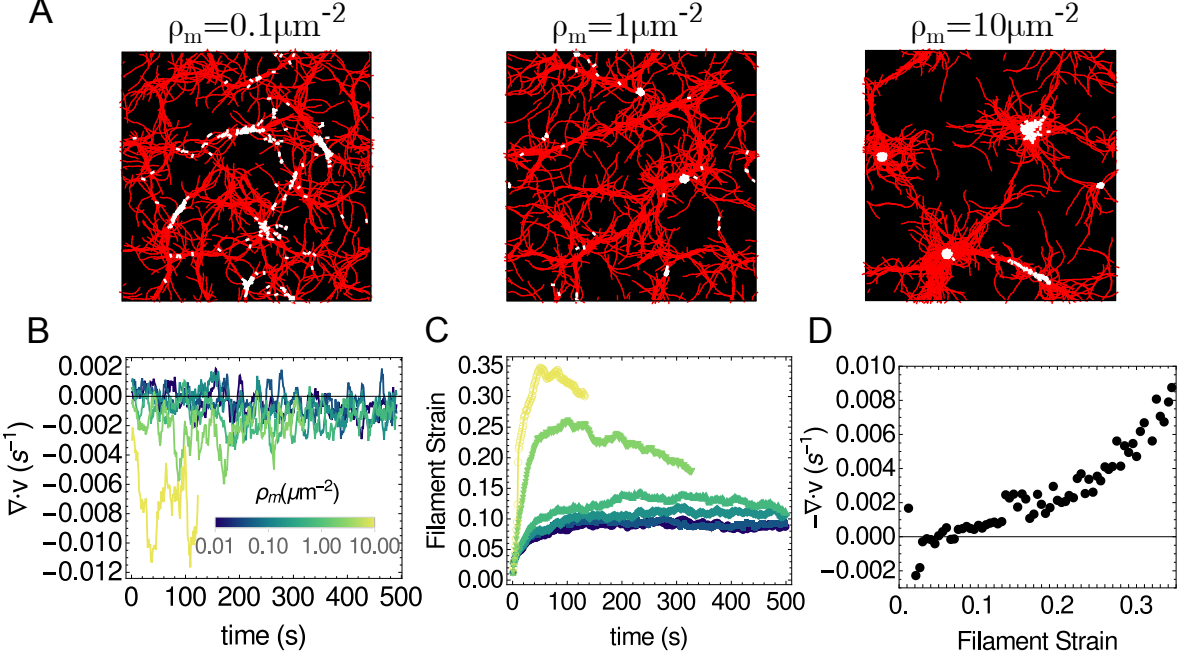


**Figure 6:** Assemblies with motors and crosslinkers yield contraction. (A) Networks configurations at their largest contractile strains for different motor densities. Filaments are shown in red, and motors in white. Only 1000 motors are shown in each case. (B) Spatially averaged divergence of filament flow field as a function of time for networks of varying motor density. Networks with a higher density of motors are more contractile. (C) Average filament strain (defined in Equation (3)) as a function of time for the same networks. (D) Correlation between filament strain and the network strain (which is measured by the negative of divergence for all times, averaged over bins of size 0.005 for all motor densities)

## 2.5 Modulating ensemble motor behavior

While the force dependent detachment and speed of an individual myosin motor is well a model input (Methods) the ensemble behavior of many motors could provide a benchmark that the simulation is capable of reproducing dynamics observed in actin motility assays [31, 32]. In a classical motility assay experiment, a layer of myosin is adhered to a plate, and actin filaments are placed on top of the motoros. Because the myosin cannot diffuse, they instead slide the actin filament across the assay. Although this experiment typically involves single myosin heads, and not myosin minifilaments, we believe that functionally the situations would be equivalent, with the substitution that each model motor head approximates the activity of dozens of single molecule myosin heads. Previous experiments [33, 34] have reported a nonlinear dependance of the speed of an actin filament across the assay on the concentration of myosin, the length of the actin filament, and the concentration of ATP in the sample. By allowing filaments to interact with more motors, one can monotonically increase the filament speed to a constant value.

To explore the dynamics of this assay, we randomly distributed motors on a  $(50 \mu\text{m})^2$  periodic simulation cell and tethered one head of each motor to its initial position. Filaments were then introduced in the simulation cell and allowed to interact with the free motor heads. The strength of motor-filament interactions was manipulated in three ways: by varying the motor concentration  $\rho_m$ , the filament contour length  $L$ , and the duty ratio  $r_D = k_m^{on}/(k_m^{on} + k_m^{off})$ . The results are shown in Figure 7, where we have used the dimensionless control parameter  $\mathcal{M} = \rho_m L^2 r_D$  representing the average number of bound motor heads, to tune filament motility.

Our findings are qualitatively similar to the previously reported experimental results. At

low  $\mathcal{M}$ , i.e., low motor density, filament length and duty ratio, transverse filament fluctuations dominate over longitudinal motion as the filament is not being propelled by motors faster than diffusion (Figure 7B). However, as  $\mathcal{M}$  is increased, longitudinal motion dominates. This can be inferred from the dependence of the mean squared displacement, plotted in Figure 7(D), where low  $\mathcal{M}$  yields diffusive behavior with an  $\langle r^2 \rangle \propto t$ , and the motion becomes ballistic with  $\langle r^2 \rangle \propto t^2$  as  $\mathcal{M}$  approaches 100. The longitudinal speed of the filament plateaus at  $v_{||} \approx 1\mu\text{m}/\text{s}$  which is the average unloaded speed of a single motor head [35]. Figure 7(C) shows that aside from being propelled, filaments are also buckled in the presence of a large number of motors, as filament strain increases with increasing  $\rho_m L^2 r_D$ . Although there are no explicit crosslinkers, at a high enough concentration, motors near the barbed end of a filament will pin the filaments for a short time, and induce buckling the same way crosslinkers do in contractile networks, similar to the effects observed in experiment [36].

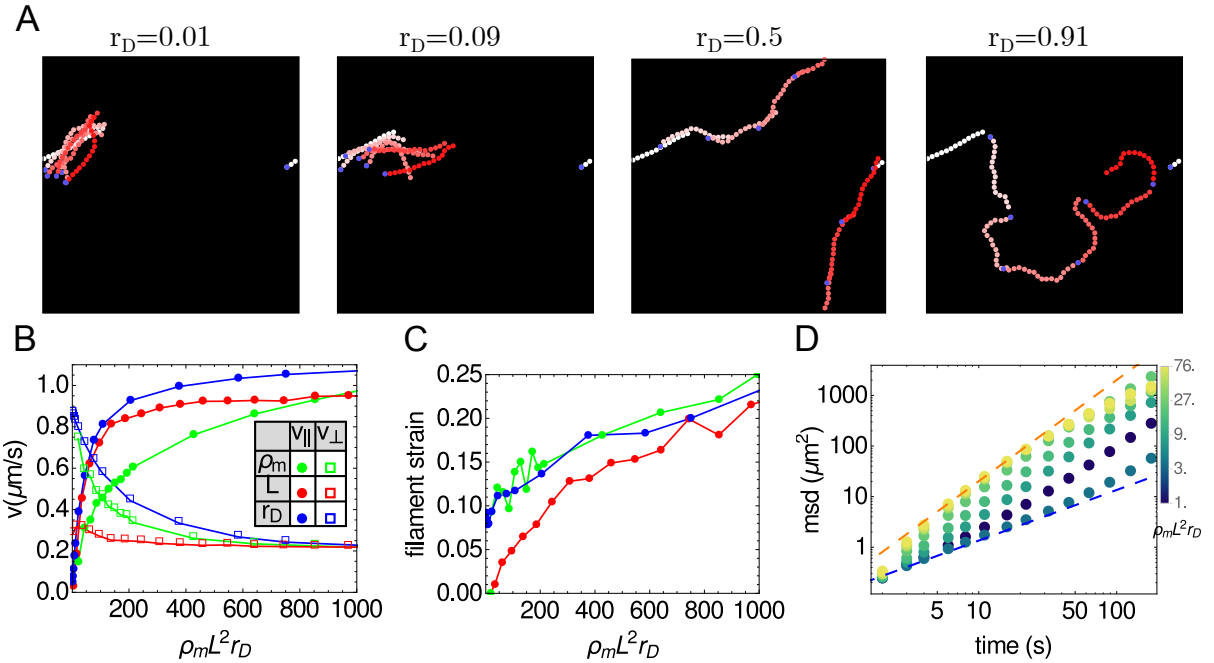


**Figure 7:** (A) Position of a filament for  $\rho_m = 10\mu\text{m}^{-2}$  and  $L = 16\mu\text{m}$  for different values of the duty ratio. White filament is the configuration at  $t = 0$  and dark red represents  $t = 90\text{s}$ . Blue dot marks the barbed end of filaments. (B) Longitudinal filament speed (circles) monotonically increases to a plateau while transverse speed (squares) decreases with larger motor density, filament length, and duty ratio. Green:  $\rho$  variable,  $L = 15\mu\text{m}$ ,  $r_D = 0.95$ ; Red:  $\rho_m = 4\mu\text{m}^{-2}$ ,  $L$  variable,  $r_D = 0.95$ ; Blue:  $\rho_m = 10\mu\text{m}^{-2}$ ,  $L = 15\mu\text{m}$ ,  $r_D$  variable. (C) Filament strain, defined in Equation (3), as a function of dimensionless parameter, indicates that the filament is being buckled during motor induced propulsions. (D) Mean squared displacement for various values of  $\rho_m L^2 r_D$  shows that the transition from diffusive (blue dashed line) to ballistic (red dashed line) behavior occurs at low values of this parameter.

### 3 Discussion

The goal of this paper is to introduce a framework that could accurately and efficiently simulate active networks of filaments, motors, and crosslinker proteins and predict the various structural and mechanical phases of the system. In doing so, we have shown that our model can reproduce the key results of canonical *in vitro* experiments involving F-actin, myosin, and crosslinks. We show that our simulated networks exhibit tunable strain stiffening upon shear, and networks

with dynamic crosslinks form bundles depending on turnover rate. In simulated actin motility assays, the filament speed scaled with attachment probability, as seen in experiment. Networks with motors are sorted by polarity, and networks with motors and crosslinks robustly contract.

For crosslinked networks, we showed that the scaling of strain stiffening can be tuned by changing the crosslinker stiffness. Many other models have successfully explained the viscoelastic properties of crosslinked actin networks [16–19, 37]. For example, Head, et al., performed simulations with straight rod filaments, and bending potentials at rod intersections, and was able to identify three distinct elastic regimes, characterized by the mean distance between crosslinkers and the temperature [17]. Similar models used non-Hookean crosslinkers to show how unfolding can yield strain softening at large strain [38]. Others, using 3D models, with explicit filament bending have examined the frequency dependence of these networks and reproduced theoretical predictions [19, 39]. Here, we have shown that by modeling crosslinkers as idealized Hookean springs, one can modulate the mechanical properties of the network by tuning it from a liquid-like material to strain stiffening elastic materials. This is particularly interesting, given that recent experimental findings suggest that one can engineer actin binding proteins of varying stiffness [40].

The ensemble motion of a many myosin motors with respect to a single actin filament has also been studied via simulation, in order to develop a realistic model of a myosin minifilament. Erdmann and Schwarz, who used Monte Carlo simulations to verify a master equation that expresses the probability that  $N$  motors are bound at time  $t$  to a single filament [21] were able to make accurate predictions for the duty ratio and force velocity curves for myosin minifilaments. Stam et al. used simulations to study force buildup on a single filament by a multi-headed motor and found distinct timescale regimes over which different molecular motors could exert force and act as crosslinkers [22]. These models of actin-myosin interaction are important to understand the mechanics at the level of a single filament, and their results can be incorporated into larger network simulations. However, our results show that even a minimal model of actin and myosin is able to capture the ballistic, longitudinally processive behavior of actin filaments in a canonical motility assay experiment.

Other actomyosin models have explored the driving mechanisms behind contractility. Dasanyake, et. al., extended the model in [17] to include a term in the potential energy that corresponded to myosin motor activity, and observed the emergence of force chains that transmit stress throughout the network [5]. Wang and Wolynes [6] model the F-actin networks as a graph of crosslinkers (nodes) and rigid actin filaments (edges) in which myosin motor activity is simulated via antisymmetric kicks along the filaments and predict a binary phase diagram of networks which are either contractile or not as a function of cross linker and myosin densities. While the simplicity of these models is intriguing, they do not account for explicit filament buckling, and their integration is performed via Monte Carlo, more applicable to structure formation than dynamics. We have shown that using an agent based model we can reproduce the experimentally observed contractility of actomyosin networks, that it scales with motor density, and that it correlates with filament buckling, both of which have been confirmed in *in vitro* reconstitutions [1, 2].

Contractility and structure formation has also been explored in the context of agent based models. Nedelec used dynamic simulations of ensembles of filaments and motor proteins to explore aster formation in microtubule-kinesin assemblies, as well as motility and contractility in actomyosin [4, 7, 20]. Kim used an agent based approach of filaments, motors and crosslinkers, to explore a variety of topics, including bundling in crosslinked networks and force generation by myosin motors [24, 41]. While the bundling observed in [41] was the result of crosslinkers that explicitly bind parallel filaments, we have that generic crosslinking leads to

network coarsening and that this bundling effect depends strongly, and non-monotonically on the crosslinker-filament affinity. These bundled networks have the important physical property of being able to transmit forces large distances, and are thought to serve the biomechanical functionality of forming force chains to propagate stress throughout the cell.

Additionally, we showed that we can tune polarity sorting in filament assemblies. Polarity sorted networks can be used to by load-carrying motors to transmit cellular goods large distances, so insight into how a cell modulates this behavior could be extremely helpful in biophysics and active matter. While this polarity sorting is similar to the aster formation seen in [4, 23], we have shown that the process will also occur when filaments are semiflexible, have developed a reliable order parameter for measuring this process, and shown that the magnitude of this parameter increases monotonically with motor density.

While our model is thorough in what it aims to simulate it is limited by a few experimental observations that are currently not implemented. First, the structure of myosin minifilaments is significantly more complex than a two headed spring. As mentioned, these minifilaments have dozens of heads, which allows them to walk along multiple filaments and could result in subdiffusive behavior [42] and significantly increase local network elasticity [43]. Another limitation of our system is that the actin filaments are static, and will not polymerize, depolymerize or sever. Within actomyosin assays it is clear that recycling of actin monomers and to a lesser degree, filament severing plays an important role in contraction [1]. Within the cytoskeleton, actin treadmilling is also important for shape production. Additionally, these simulations are all run in  $2D$  and without steric interactions, and dimensionality and volume exclusion may play important roles. While we intend to address and investigate these limitations in future works, we believe that the successful benchmarking of the simulation at various levels is a significant argument in favor of the current setup.

There are still many unanswered questions regarding self-organization in actomyosin networks that we hope can be addressed using this simulation, such as how actomyosin controls the shape of cell membranes, and how they form force propagating chains across the cytoskeleton [5, 44]. In particular, it is significantly easier to measure internal active forces and energies in simulation than in experiment, so we expect this model will aid the process of isolating the particular mechanisms involved in restructuring these polymer assemblies. We stress, however, that the applicability of such a simulation package reaches beyond studying the phases of actomyosin networks. We believe this simulation can shed light on the mechanics and dynamics of a variety of active polymer assemblies.

Similar networks that involve other proteins also exist in the cytoskeleton, such as microtubule-kinesin-dynein networks and could be investigated using this simulation methodology. Furthermore, the cytoskeleton demonstrates how populations of simple machines can self assemble into active materials with useful mechanical properties, and one can use this simulation to efficiently design these types of self assembled materials. Thus, the non-equilibrium molecular dynamics framework of this simulation can be used to model and study many open questions in active matter and biophysics.

## 4 Methods

### 4.1 Actin Filaments

Actin filaments are treated as a worm-like chain, with each filament represented as a set of  $N+1$  beads connected by  $N$  harmonic springs (links), with an additional harmonic angular potential applied on the  $N - 1$  angles along the chain, as depicted in Figure 8(A). The linear springs

penalize stretching of individual subunits and the  $N - 1$  angular harmonic springs penalize bending and enforce the length scale over which the filaments are semi-flexible.

The internal forces on actin filaments can be obtained from the gradient of the potential energy  $U_f$

$$U_f = U_{stretch} + U_{bend} \quad (4)$$

$$U_{stretch} = \frac{k_a}{2} \sum_{i=1}^N (|d_i| - l_a)^2 \quad (5)$$

$$U_{bend} = \frac{\kappa_B}{2l_a} \sum_{i=2}^N \theta_i^2$$

where  $d_i = r_i - r_{i-1}$ ,  $\theta_i = \arccos\left(\frac{d_i \cdot d_{i-1}}{|d_i||d_{i-1}|}\right)$ ,  $k_a$  is the stretching force constant,  $\kappa_B$  is the bending modulus, and  $l_a$  is the equilibrium length of a link.

For a confined semiflexible filament, it has been shown that for a polymer of a given persistence length  $L_p$ , the shortest length that should be considered as unbending ( $l_a$ ) is given by  $l_a \approx A^{2/3} L_p^{1/3}$  where  $A$  is a length scale associated with the confinement of the filament [45]. In these simulations, filaments were confined by nearby motors and crosslinkers. Since the smallest motor or crosslinker density used was  $\rho_m = 0.1 \mu m^{-2}$ ,  $A \geq 1/\sqrt{0.1 \mu m^{-2}} \Rightarrow l_a \geq 5 \mu m$ . In general, we used  $l_a = 1 \mu m$ . The bending force constant is derived from the persistence length  $L_p$  such that  $\kappa_B = L_p k_B T$  where  $k_B$  is Boltzmann's constant and  $T$  is the temperature [46]. Experimentally, the stretching force constant has been measured to be in the approximate range  $k_a = 40 - 70 pN/nm$  [47, 48]; however, simulating a network of filaments with this large of a stiffness is computationally inefficient since the maximum timestep of a simulation is inversely proportional to the largest stiffness in the simulation. Therefore, we chose  $\frac{\kappa_B}{l_a} \ll k_a$ , so that the filaments were still much easier to bend than to stretch, enabling us to run simulations of experimentally relevant dimension. We show that our simple filament model exhibits expected behavior for a semiflexible filament in the next section and we have further verified that  $k_a$  did not effect the persistence length of the filament, as seen in Section 6.2.1.

Since actin bending is instrumental for actomyosin contraction, and simulating precise bending moduli is non-trivial, we tested our filaments by measuring spatial and temporal fluctuations and comparing with theoretical predictions. In a two dimensional WLC, a bending of two adjacent segments is expected to result in a local change in free energy of  $\frac{\kappa_B}{2l_a \theta_i^2}$ , and it is predicted that [49]

$$\langle \theta^2(l) \rangle = \frac{l}{L_p} \quad (6)$$

$$\langle \cos(\theta(l)) \rangle = \exp(-l/2L_p) \quad (7)$$

where  $\theta(l) = \theta_j - \theta_i$  where  $1 < i < j \leq N$ ,  $l = l_a(j-i)$  and  $L_p$  is the persistence length. To test our model against these equations, we simulate 100 filaments of  $L = 200 \mu m$  and  $\kappa_B = 0.08 pN \mu m^2$  at  $T = 300 K$  for  $T_f = 100 s$  and measured the resulting filament configuration every 1 s. We discard the first 10 seconds of each simulation to allow equilibration, and we used only the middle  $150 \mu m$  of the filament to calculate these correlation functions. Figure S1(a) shows that the measured persistence length, obtained by performing a least squares fit to plots of  $\log(\langle \cos(\theta(l)) \rangle)$  for various values of  $\kappa_B$  yields the expected result over at least 3 orders of magnitude. Further measurements of the persistence length as well as verifications of its independence on other filament parameters is available in the supplement Section 6.2.

An additional prediction for semiflexible filaments is the scaling of fluctuations with time. Fluctuations transverse to the filament orientation have been shown to increase as a function of

time as  $\langle dr_{\perp}^2 \rangle \propto t^{3/4}$  while longitudinal fluctuations have been shown to follow the power law  $\langle dr_{\parallel}^2 \rangle \propto t^{7/8}$  [50]. To test these predictions, we followed the procedure outlined in [50] and generated  $N = 100$  initial filament configurations of a  $20\mu\text{m}$  filament. For each configuration we ran  $M = 100$  simulations of the filament fluctuating for 1s. At each time step we collected the  $2N$  positions of the filament ends,  $r_e(t)$ . We then calculated the eigenvalues of the covariance matrix  $\text{cov}(r_e(t) \cdot \hat{i}, r_e(t) \cdot \hat{j})$  where  $i, j \in \{x, y\}$ . The larger eigenvalue  $\lambda_1(t)$  corresponds to the slower longitudinal fluctuations (i.e.,  $\lambda_1(t) \propto t^{7/8}$ ) while the smaller eigenvalue corresponded to the faster perpendicular fluctuations ( $\lambda_2(t) \propto t^{3/4}$ ). We show in Figure 8(C) that our simulation exhibits scaling of these eigenvalues in good agreement with the prediction of Ref. [50].

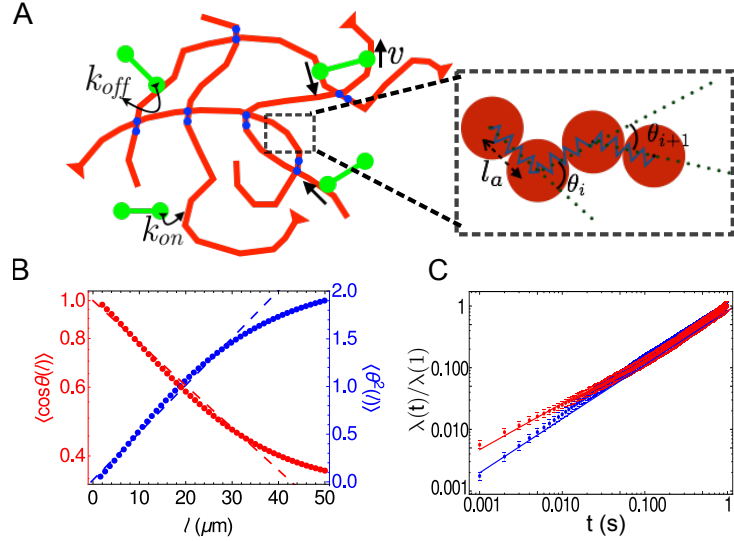


**Figure 8:** (A) Sketch of semiflexible filaments (red); motors (green) binding, unbinding, and walking; and crosslinkers (blue) connecting filament intersections. Zoom in of the filament model shows a segment of the bead spring chain, identifying the angle used in Section 4.1. (B) Decorrelation of tangent vectors (red dots) and fluctuations in angles between links (blue dots) as a function of the arc length between them. Red dashed line is  $e^{-s/2L_p}$  shows the expected behavior from the input bending modulus of  $0.08pN - \mu\text{m}^2$  and blue dashed line has slope  $1/L_p$ . (C) Eigenvalues of covariance matrices for the positions of endpoints of filaments as a function of time. We analyze fluctuations of  $N = 100$  filaments, with each point the average over the  $2N$  eigenvalues for  $\lambda_1(t)$  and  $\lambda_2(t)$  and error bars showing the standard deviations for the distribution of these values. Blue dots shows the longitudinal fluctuations and the red dots shows the transverse fluctuations. Red dashed line is  $t^{3/4}$  and blue dashed line is  $t^{7/8}$  as predicted by [50].

## 4.2 Crosslinkers

Crosslinker proteins dynamically connect actin filaments, thereby propagating force from one to another. Thus model crosslinkers, must be able to attach and detach from actin filaments, and be compliant in order to propagate force. They are therefore modeled as hookean springs, with stiffness  $k_{cl}$  and rest length  $l_{cl}$ . Like actin filaments, the Young's modulus of most crosslinkers is significantly higher than would be reasonable to simulate; therefore we set  $k_{cl} = 1-100pN/\mu\text{m}$  was so that the bending mode of actin filaments was significantly softer than the stretching mode of crosslinkers. Their rest length  $l_{cl}$  differs by the type of cross-linker and ranges from 10nm for fascin to 150nm for filamin.

At each time step of the simulation an unattached crosslinker head is allowed to attach

to nearby filaments and an attached crosslinker head can detach. The probability of a head attaching to an actin filament is a Gaussian distributed random variable, such that

$$P_{cl}^{on} = k_{cl}^{on} dt \exp(-r^2/R^2) \quad (8)$$

where  $r$  is the shortest distance from the head to the actin filament and  $R = \sqrt{\frac{2k_B T}{k_{cl}}}$  where  $k_B$  is Boltzmann's constant and  $T$  is the temperature. For crosslinker detachment we assume that the behavior is that of a slip bond, such that a higher tensile force along the crosslinker backbone will result in a higher probability of detachment. Thus,

$$P_{cl}^{off} = k_{cl}^{off} dt \exp(Fx_{cl}/k_B T) \quad (9)$$

where  $F$  is the force along the crosslinker backbone, and  $x_{cl}$  is a characteristic bond length [22].

When a crosslinker is bound to a filaments at both ends, it will necessarily be stretched or compressed. If it were allowed to relax independently of the actin filaments to which it is bound, it would no longer lie on those filaments. Therefore, the tensile force stored on a stretched or compressed crosslinker is propagated onto those actin filaments via the lever rule outlined in [4, 23]. Thus, if the tensile force of a motor at point  $r_j$  between filament beads  $i$  and  $i + 1$  is  $F_{cl}$ , then,

$$\begin{aligned} F_i &= F_{cl} \left| \left( \frac{r_j - r_i}{r_{i+1} - r_i} \right) \right| \\ F_{i+1} &= F - F_i \end{aligned} \quad (10)$$

will be the forces on beads  $i$  and  $i + 1$  respectively due to the crosslinker.

### 4.3 Motors

Within the cytoskeleton, tens of myosin II motors aggregate into bipolar ensembles called myosin minifilaments [22]. While the mechanochemical process through which individual myosin motors walk along actin filaments is complex, motility assay experiments have shown that on average bound myosin II heads walk at an unloaded speed of  $v_0 \approx 1\mu m/s$  along actin filaments [51]. To a first approximation, minifilaments therefore should also have a mean speed of  $1\mu m/s$  (although see [22] and [32] for higher order measurements). Since myosin also functions to increase the local elasticity of networks wherever it is bound, the myosin is modeled similarly to a crosslinker, in that it behaves like a hookean spring with two heads, a stiffness  $k_m$  and a rest length  $l_m$ . It should be noted, however, that the two heads of this spring do not correspond directly to individual molecular myosin heads; rather each of them represents tens of myosin molecules, and their rate constants will reflect that notion. It would be undesirable for a myosin minifilament to stretch, since experimentally they have a very high Young's modulus and it is unlikely that their length would change noticeably in the cytoskeleton. Thus we set  $k_m \gg \kappa_B/l_a$  so that the bending of actin is still the softest mode. The rest length was set to the average length of minifilaments [52]. Attachment and detachment kinetics for motors are the same as for crosslinkers, subscripted with  $m$  instead of  $cl$  in Equations (8) and (9). One extra parameter is needed  $k_m^{end}$  for the detachment of myosin from the barbed end of a filament, as detachment from the end is significantly more probable than from the rest of the filament. Similarly, force propagation onto minifilaments is done using the lever rule described in Section 4.2.

Unlike crosslinkers, motors process towards the barbed end of actin filaments to which they are bound at speeds that vary depending on the tensile force along the crosslinker. The

relationship between motor velocity and tensile force is modeled linearly, such that the motor head will speed up if the minifilament is compressed (pre-powerstroke) and slow down if the minifilament is stretched (post powerstroke) going to 0 when the force on the minifilament is the stall force  $F_s \approx 3.85pN$  [4, 23]; i.e.,

$$v(F_{||}) = v_0 \left( 1 - \frac{F_{||}}{F_s} \right) \quad (11)$$

where  $F_{||}$  is the force on the motor, projected along the tangent vector of the actin filaments. The minor differences between crosslinkers and motors allow us treat them equivalently, by setting  $v_0 = 0$  for the crosslinkers.

## 4.4 Dynamics

We Langevin dynamics to solve for the motion of actin filaments, myosin minifilaments and crosslinkers. The Langevin equations of motion for a spherical bead of mass  $m$  and radius  $R$  at position  $r(t)$  at time  $t$  can be written,

$$m\ddot{r}(t) = F(t) + B(t) - 4\pi R\nu\dot{r}(t) \quad (12)$$

where  $F(t)$  is the force on the particle due to its interactions and  $B(t)$  is Brownian forcing term, to simulate a temperature,  $\nu$  is the dynamic viscosity of the bead's environment, and we have used the Einstein relation for the damping term. Since the fastest motion in this simulation is that of the myosin, and a  $0.4\mu m$  myosin minifilament moving at a speed of  $1\mu m/s$  in a liquid at least as viscous as water ( $\nu_D = 10^6\mu m^2/s$  dynamic viscosity) has a very low Reynold's number ( $Re \approx 4 * 10^{-7}$ ) we can treat the dynamics in the overdamped limit where the equation of motion is Equation (12) without the acceleration term, i.e. with  $m = 0$ . Furthermore, in the limit of small  $\Delta t$ , we may write  $\dot{r}(t) \approx \frac{r(t+\Delta t) - r(t)}{\Delta t}$ . These two approximations allow us to rewrite Equation (12) as

$$r(t + \Delta t) = r(t) + F(t)\mu\Delta t + B(t)\mu\Delta t \quad (13)$$

where  $\mu = (4\pi R\nu)^{-1}$ . For the Brownian term, we use the form of Leimkuhler and Matthews [53, 54] that has been shown to minimize deviations from canonical averages in harmonic systems,

$$B(t) = \sqrt{\frac{2k_B T}{\mu\Delta t}} \left( \frac{W(t) + W(t - \Delta t)}{2} \right) \quad (14)$$

where  $W(t)$  is a Wiener process, in this case a random number drawn from the normal distribution with mean zero and standard deviation of unity.

## 4.5 Environment

Because the probability of motor attachment decays as a Gaussian function of distance from the filament, it would be highly inefficient to attempt motor attachments with every filament in the simulation. Rather, we choose to test for connections only within a cutoff distance  $r_c > 3R/2$  (where  $R$  is defined above as in Equation (8)). A grid of lattice size  $2r_c$  is drawn in the  $2D$  plane of the simulation, and the position of a filament is approximated as the points on the grid nearest to the beads of the filament. Thus, to determine if a motor will bind to a filament at time  $t$ , it is sufficient to only attempt attachment to filaments that are indexed at the four nearest grid points to a motor.

In general, we use periodic boundary conditions so as to limit effects of a boundary and to mimic a system larger than the one we simulate. Lees-Edwards boundaries [29] were used for shearing simulations, and hard wall boundaries have also been implemented. The value for  $\Delta t$  in Equation (13) generally depends on both the unloaded myosin speed  $v_0$  and the largest stiffness in the simulation  $k_f$ . For  $k_f = 10\text{pN}/\mu\text{m}$  and  $v_0 = 1\mu\text{m}/\text{s}$  a value of  $\Delta t = 0.00001\text{s}$  was sufficiently low to solve Equation (13) for hundreds of seconds without spuriously generating configurations of very large energy. The length and width of the simulations were chosen so as to be high enough to avoid boundary artifacts. A complete list of simulation parameters used throughout this article is provided in Table 1.

## 5 Acknowledgements

We thank M. Gardel, J. Weare, C. Matthews, F. Nedelev, F. Mackintosh, and M. Murrell for helpful conversations. This research was supported in part by the University of Chicago Materials Research Science and Engineering Center (NSF Grant No. 1420709). S.L.F. was supported by the Department of Defense (DoD) through the National Defense Science & Engineering Graduate Fellowship (NDSEG) Program. G.M.H. was supported by an NIH Ruth L. Kirschstein NRSA award (1F32GM113415-01).

## References

- [1] Michael P. Murrell and Margaret L. Gardel. F-actin buckling coordinates contractility and severing in a biomimetic actomyosin cortex. *Proceedings of the National Academy of Sciences*, 109(51):20820–20825, 2012.
- [2] Michael Murrell and Margaret L. Gardel. Actomyosin sliding is attenuated in contractile biomimetic cortices. *Molecular Biology of the Cell*, 25(12):1845–1853, 2014.
- [3] Kingo Takiguchi. Heavy meromyosin induces sliding movements between antiparallel actin filaments. *Journal of biochemistry*, 109(4):520–527, 1991.
- [4] François Nédélec. Computer simulations reveal motor properties generating stable antiparallel microtubule interactions. *The Journal of Cell Biology*, 158(6):1005–1015, 2002.
- [5] Nilushi L. Dasanayake, Paul J. Michalski, and Anders E. Carlsson. General mechanism of actomyosin contractility. *Physical Review Letters*, 107(11):118101, 2011.
- [6] Shenshen Wang and Peter G. Wolynes. Active contractility in actomyosin networks. *Proceedings of the National Academy of Sciences*, 109(17):6446–6451, 2012.
- [7] Hajar Ennmani, Gaëlle Letort, Christophe Guérin, Jean-Louis Martiel, Wenxiang Cao, François Nédélec, M Enrique, Manuel Théry, and Laurent Blanchoin. Architecture and connectivity govern actin network contractility. *Current Biology*, 26(5):616–626, 2016.
- [8] H.E. Huxley. The mechanism of muscular contraction. *Science*, 164(3886):1356–1366, 1969.
- [9] Martin Lenz, Todd Thoresen, Margaret L Gardel, and Aaron R Dinner. Contractile units in disordered actomyosin bundles arise from f-actin buckling. *Physical review letters*, 108(23):238107, 2012.

**Table 1:** Parameter Values

Symbol	Description (units) [ref]	$L_p$	Shear	Motility Assay	Networks
<b>Actin Filaments</b>					
$N_B$	Number of beads	21 – 201	16	16	16
$l_a$	Link Rest Length ( $\mu m$ ) [45]	1	1	1	1
$k_a$	Stretching Force Constant ( $pN/\mu m$ )	0.01 – 10	10	1	1
$\kappa_B$	Bending Modulus ( $pN\mu m^2$ ) [55]	0.002 – 5	0.08	0.08	0.08
<b>Myosin Minifilaments</b>					
$l_m$	Rest Length ( $\mu m$ ) [52]	n/a	n/a	0.5	0.5
$k_m$	Stiffness ( $pN/\mu m$ )	n/a	n/a	1	1
$k_m^{on}$	Attachment rate at distance $r = 0$ ( $s^{-1}$ )	n/a	n/a	2 – 4000	3600
$k_m^{off}$	Unloaded head detachment rate ( $s^{-1}$ )	n/a	n/a	200	200
$k_m^{end}$	Unloaded head detachment rate at the barbed end of the filament ( $s^{-1}$ )	n/a	n/a	2000	2000
$x_m$	characteristic bond length ( $\mu m$ ) [22]	n/a	n/a	0.0004	0.0004
$v_0$	Unloaded speed ( $\mu m/s$ ) [35]	n/a	n/a	1	1
$F_s$	Stall force of myosin ( $pN$ ) [56]	n/a	n/a	3.85	3.85
<b>Crosslinkers</b>					
$l_{cl}$	Rest Length (Filamin) ( $\mu m$ ) [57]	n/a	0.150	n/a	0.150
$k_{cl}$	Stiffness ( $pN/\mu m$ )	n/a	1, 10	n/a	1
$k_{cl}^{on}$	Attachment rate at distance $r = 0$ ( $s^{-1}$ )	n/a	$10^6, 10^5$	n/a	3600
$k_{cl}^{off}$	Unloaded head detachment rate ( $s^{-1}$ )	n/a	0	n/a	0.2
$x_{cl}$	characteristic bond length ( $\mu m$ )	n/a	0.0004	0.0004	0.0004
<b>Environment</b>					
$dt$	Dynamics timestep (s)	$10^{-4}$	$10^{-6}, 10^{-5}$	$2.5 \times 10^{-4}$	$2.5 \times 10^{-4}$
$T_F$	total simulated time (s)	100	0.5	100	500
$X, Y$	Length and width of assay ( $\mu m$ )	n/a	75	50	75
$r_c$	Mesh (actomyosin binding site) size ( $\mu m$ )	n/a	0.2	0.2	0.2
$T$	$k_B * \text{Temperature}$ ( $pN\mu m$ )	0.004	0.004	0.004	0.004
$\nu$	Dynamic viscosity ( $mg/(\mu ms)$ )	0.001	0.001	0.001	0.001
$\gamma$	Strain (%) [58]	n/a	0.001	n/a	n/a
$t_{relax}$	Amount of time between sequential strains (s)	n/a	0.001	n/a	n/a

- [10] Michael Murrell, Patrick W. Oakes, Martin Lenz, and Margaret L. Gardel. Forcing cells into shape: the mechanics of actomyosin contractility. *Nature Reviews Molecular Cell Biology*, 16(8):486–498, 2015.
- [11] Samantha Stam, Shiladitya Banerjee, Simon Freedman, Kimberly Weirich, Aaron R Dinner, and Margaret L Gardel. Filament rigidity and connectivity tune the deformation modes of active cytoskeletal networks. *in preparation*.
- [12] Stanislav Burov, S.M. Ali Tabei, Toan Huynh, Michael P. Murrell, Louis H. Philipson, Stuart A. Rice, Margaret L. Gardel, Norbert F. Scherer, and Aaron R. Dinner. Distribution of directional change as a signature of complex dynamics. *Proceedings of the National Academy of Sciences*, 110(49):19689–19694, 2013.
- [13] M.L. Gardel, J.H. Shin, F.C. MacKintosh, L. Mahadevan, P. Matsudaira, and D.A. Weitz. Elastic behavior of cross-linked and bundled actin networks. *Science*, 304(5675):1301–1305, 2004.
- [14] Minakshi Guha, Mian Zhou, and Yu-li Wang. Cortical actin turnover during cytokinesis requires myosin ii. *Current biology*, 15(8):732–736, 2005.
- [15] Cyrus A Wilson, Mark A Tsuchida, Greg M Allen, Erin L Barnhart, Kathryn T Applegate, Patricia T Yam, Lin Ji, Kinneret Keren, Gaudenz Danuser, and Julie A Theriot. Myosin ii contributes to cell-scale actin network treadmilling through network disassembly. *Nature*, 465(7296):373–377, 2010.
- [16] F.C. MacKintosh, J. Käs, and P.A. Janmey. Elasticity of semiflexible biopolymer networks. *Physical Review Letters*, 75(24):4425, 1995.
- [17] D. A. Head, A. J. Levine, and F. C. MacKintosh. Distinct regimes of elastic response and deformation modes of cross-linked cytoskeletal and semiflexible polymer networks. *Phys. Rev. E*, 68:061907, Dec 2003.
- [18] Jan Wilhelm and Erwin Frey. Elasticity of stiff polymer networks. *Physical Review Letters*, 91(10):108103, 2003.
- [19] Taeyoon Kim, Wonmuk Hwang, Hyungsuk Lee, and Roger D. Kamm. Computational analysis of viscoelastic properties of crosslinked actin networks. 2009.
- [20] Francois Nedelec and Dietrich Foethke. Collective langevin dynamics of flexible cytoskeletal fibers. *New Journal of Physics*, 9(11):427, 2007.
- [21] Thorsten Erdmann and Ulrich S. Schwarz. Stochastic force generation by small ensembles of myosin ii motors. *Physical Review Letters*, 108(18):188101, 2012.
- [22] Samantha Stam, Jon Alberts, Margaret L. Gardel, and Edwin Munro. Isoforms confer characteristic force generation and mechanosensation by myosin ii filaments. *Biophysical journal*, 108(8):1997–2006, 2015.
- [23] Daniel Gordon, Anne Bernheim-Groswasser, Chen Keasar, and Oded Farago. Hierarchical self-organization of cytoskeletal active networks. *Physical Biology*, 9(2):026005, 2012.

- [24] Taeyoon Kim. Determinants of contractile forces generated in disorganized actomyosin bundles. *Biomechanics and modeling in mechanobiology*, 14(2):345–355, 2014.
- [25] G.H. Koenderink, M. Atakhorrami, F.C. MacKintosh, and C.F. Schmidt. High-frequency stress relaxation in semiflexible polymer solutions and networks. *Physical Review Letters*, 96(13):138307, 2006.
- [26] KE Kasza, GH Koenderink, YC Lin, CP Broedersz, W Messner, F Nakamura, TP Stossel, FC MacKintosh, and DA Weitz. Nonlinear elasticity of stiff biopolymers connected by flexible linkers. *Physical Review E*, 79(4):041928, 2009.
- [27] Yi-Chia Lin, Norman Y. Yao, Chase P. Broedersz, Harald Herrmann, Fred C. MacKintosh, and David A. Weitz. Origins of elasticity in intermediate filament networks. *Physical Review Letters*, 104(5):058101, 2010.
- [28] Denis J. Evans and G.P. Morriss. Nonlinear-response theory for steady planar couette flow. *Physical Review A.*, 30(3):1528, 1984.
- [29] Mike P. Allen and Dominic J. Tildesley. *Computer simulation of liquids*. Oxford university press, 1989.
- [30] Yair Shokef and Samuel A Safran. Scaling laws for the response of nonlinear elastic media with implications for cell mechanics. *Physical review letters*, 108(17):178103, 2012.
- [31] Daniel Riveline, Albrecht Ott, Frank Jülicher, Donald A Winkelmann, Olivier Cardoso, Jean-Jacques Lacapère, Soffia Magnúsdóttir, Jean-Louis Viovy, Laurence Gorre-Talini, and Jacques Prost. Acting on actin: the electric motility assay. *European biophysics journal*, 27(4):403–408, 1998.
- [32] Sam Walcott, David M. Warshaw, and Edward P. Debold. Mechanical coupling between myosin molecules causes differences between ensemble and single-molecule measurements. *Biophysical journal*, 103(3):501–510, 2012.
- [33] David E. Harris and D.M. Warshaw. Smooth and skeletal muscle myosin both exhibit low duty cycles at zero load in vitro. *Journal of Biological Chemistry*, 268(20):14764–14768, 1993.
- [34] Seiji Umemoto and James R Sellers. Characterization of in vitro motility assays using smooth muscle and cytoplasmic myosins. *Journal of Biological Chemistry*, 265(25):14864–14869, 1990.
- [35] Stephen J. Kron and James A. Spudich. Fluorescent actin filaments move on myosin fixed to a glass surface. *Proceedings of the National Academy of Sciences*, 83(17):6272–6276, 1986.
- [36] Volker Schaller, Christoph Weber, Christine Semmrich, Erwin Frey, and Andreas R Bausch. Polar patterns of driven filaments. *Nature*, 467(7311):73–77, 2010.
- [37] F. Gittes and F.C. MacKintosh. Dynamic shear modulus of a semiflexible polymer network. *Physical Review E*, 58(2):R1241, 1998.
- [38] BA DiDonna and Alex J Levine. Unfolding cross-linkers as rheology regulators in f-actin networks. *Physical Review E*, 75(4):041909, 2007.

- [39] Kei W Müller, Robijn F Bruinsma, Oliver Lieleg, Andreas R Bausch, Wolfgang A Wall, and Alex J Levine. Rheology of semiflexible bundle networks with transient linkers. *Physical review letters*, 112(23):238102, 2014.
- [40] Jeffrey Vieregg, Michael Lueckheide, Lorraine Leon, Amanda Marciel, and Matthew Tirrell. Nucleic acid-peptide complex phase controlled by dna hybridization. *Bulletin of the American Physical Society*, 2016.
- [41] Taeyoon Kim, W Hwang, and RD Kamm. Computational analysis of a cross-linked actin-like network. *Experimental Mechanics*, 49(1):91–104, 2009.
- [42] Monika Scholz, Stanislav Burov, Kimberly L Weirich, Björn J Scholz, SM Ali Tabei, Margaret L Gardel, and Aaron R Dinner. Cycling state that can lead to glassy dynamics in intracellular transport. *Physical Review X*, 6(1):011037, 2016.
- [43] M. Murrell. personal communication.
- [44] Tamara S Fraley, Clifford B Pereira, Thuan C Tran, CoreyAyne Singleton, and Jeffrey A Greenwood. Phosphoinositide binding regulates  $\alpha$ -actinin dynamics mechanism for modulating cytoskeletal remodeling. *Journal of Biological Chemistry*, 280(15):15479–15482, 2005.
- [45] Theo Odijk. The statistics and dynamics of confined or entangled stiff polymers. *Macromolecules*, 16(8):1340–1344, 1983.
- [46] Michael Rubinstein and Ralph H. Colby. *Polymer Physics*. OUP Oxford, 2003.
- [47] H. Kojima, A. Ishijima, and T. Yanagida. Direct measurement of stiffness of single actin filaments with and without tropomyosin by in vitro nanomanipulation. *Proceedings of the National Academy of Sciences*, 91(26):12962–12966, 1994.
- [48] Hideo Higuchi, Toshio Yanagida, and Yale E. Goldman. Compliance of thin filaments in skinned fibers of rabbit skeletal muscle. *Biophysical Journal*, 69(3):1000, 1995.
- [49] C. Frontali, E. Dore, A. Ferrauto, E. Gratton, A. Bettini, M.R. Pozzan, and E. Valdevit. An absolute method for the determination of the persistence length of native dna from electron micrographs. *Biopolymers*, 18(6):1353–1373, 1979.
- [50] R. Everaers, F. Jülicher, A. Ajdari, and A.C. Maggs. Dynamic fluctuations of semiflexible filaments. *Physical Review Letters*, 82(18):3717, 1999.
- [51] Jeffrey T. Finer, Robert M. Simmons, James A. Spudich, et al. Single myosin molecule mechanics: piconewton forces and nanometre steps. *Nature*, 368(6467):113–119, 1994.
- [52] Richard Niederman and Thomas D. Pollard. Human platelet myosin. ii. in vitro assembly and structure of myosin filaments. *The Journal of Cell Biology*, 67(1):72–92, 1975.
- [53] Benedict Leimkuhler and Charles Matthews. Rational construction of stochastic numerical methods for molecular sampling. *Applied Mathematics Research eXpress*, page abs010, 2012.
- [54] Benedict Leimkuhler and Charles Matthews. Robust and efficient configurational molecular sampling via langevin dynamics. *The Journal of Chemical Physics*, 138(17):174102, 2013.

- [55] A. Ott, M. Magnasco, A. Simon, and A. Libchaber. Measurement of the persistence length of polymerized actin using fluorescence microscopy. *Physical Review E*, 48(3):R1642, 1993.
- [56] Claudia Veigel, Justin E. Molloy, Stephan Schmitz, and John Kendrick-Jones. Load-dependent kinetics of force production by smooth muscle myosin measured with optical tweezers. *Nature Cell Biology*, 5(11):980–986, 2003.
- [57] Jorge M. Ferrer, Hyungsuk Lee, Jiong Chen, Benjamin Pelz, Fumihiko Nakamura, Roger D. Kamm, and Matthew J. Lang. Measuring molecular rupture forces between single actin filaments and actin-binding proteins. *Proceedings of the National Academy of Sciences*, 105(27):9221–9226, 2008.
- [58] Jonathan Stricker, Tobias Falzone, and Margaret L. Gardel. Mechanics of the f-actin cytoskeleton. *Journal of biomechanics*, 43(1):9–14, 2010.

## 6 Supplement

### 6.1 Algorithm Pseudocode

In pseudocode we can describe each timestep of the simulation as follows

```

For Each Bead on Each Filament:
    Update force from filament stretching
    Update force from filament bending

    Update position via Equation (13)

For Each Head on each Motor (cross-linker)
    If head is unattached
        try to attach
        Add up forces (stretching)

    Update position via Equation (13)

    If head is attached
        Update position via Equation (13)

        Try to detach
        If not detached
            Step toward barbed end
            Update attached actin with stretch force
        Update neighbor lists
    
```

### 6.2 Further tests of the WLC model

From Equation (7) the distribution of the square of end to end distances can be calculated as

$$\langle r^2 \rangle = \int_0^L ds' \int_0^L ds \exp(|s - s'|)/(2L_p) = 4L_p L \left( 1 - \frac{2L_p}{L} (1 - \exp(-L/2L_p)) \right) \quad (15)$$

Thus, Equation (15) provides a third method for measuring the persistence length by averaging the observable  $r_N - r_0$ . Figure S1(d) shows the results of the end to end distributions for each of these sets of simulations for each  $L$ . We fit this data to Equation (15) to obtain a third estimate for  $L_p$ . See Section 6.2 for further detail regarding the calculation of data points, error bars, and fits in these plots. The agreement between the three fits in Figure 8(B) and Figure S1(d), and the fact that all measurements produced data in reasonable correspondance with the input persistence length,  $L_p = \kappa_B/k_B T = 20\mu m$  show that the model correctly simulates a semiflexible filament. In Figure 8(B), for each value of  $L$ , the results of the 10 simulations were averaged to give one number  $\overline{\theta_L^2(l)}$ , and a standard deviation  $\sigma(\overline{\theta_L^2(l)})$ . These values were then averaged to obtain a single value of  $\overline{\theta^2(l)} = \sigma(\theta^2(l))^2 \sum_L \frac{\overline{\theta_L^2(l)}}{\sigma(\overline{\theta_L^2(l)})^2}$  where  $\sigma(\theta^2(l))^2 = 1/\sum_L \sigma(\overline{\theta_L^2(l)})^{-2}$ . The values for the  $\overline{\theta^2(l)}$  were fit to a line via least squares and  $L_p$  was calculated as the inverse of the slope. The same process was done for the data points in the blue curve, wherein  $\ln(\overline{(\cos(\theta(l))})$  was fit to a line via least squares and  $L_p = -1/2m$  where  $m$  is the slope of the fit line. For Figure S1(d), the data point itself is the average of  $\langle r^2(L) \rangle$  over the 10 simulations, and the error bars show one standard deviation of the ensemble. The data is then fit to the nonlinear function in Equation (15) using the *Wolfram Mathematica* function *NonlinearModelFit* and a value for  $L_p$  is predicted.

### 6.2.1 Further tests of the WLC model

To verify that the persistence length was independent of the stretching stiffness  $k_f$ , we evaluated  $L_p$  using a fit to Equation (7) for various values of  $k_a$  as shown in Figure S1(b). For  $k_a > 5pN/\mu m$  we find that  $L_p$  is independent of  $k_a$ .

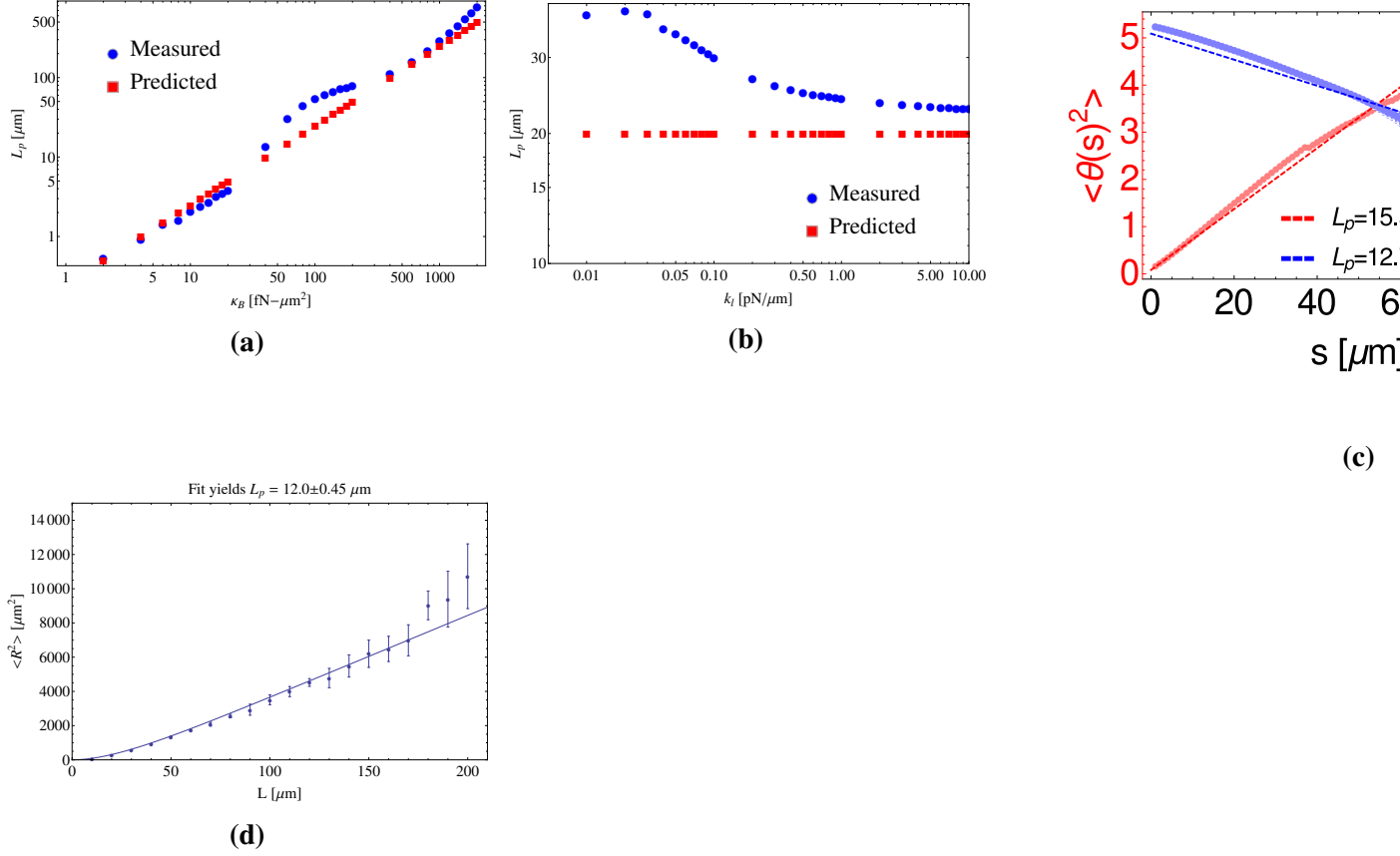


**Figure S1:** (a) Input bending modulus vs measured persistence length over three orders of magnitude. Persistence length was measured by fitting a line to  $\ln(\langle \cos(\theta) \rangle)$  in each case. (b) Persistence length as function of stretching stiffness approaches correct answer for high enough stiffness. (c) Methods 1 and 2 of measuring persistence length, described in main text using different length filaments. (d) A third method for measuring persistence length, as function of end to end distance, described above.

### 6.3 Strain Stiffening

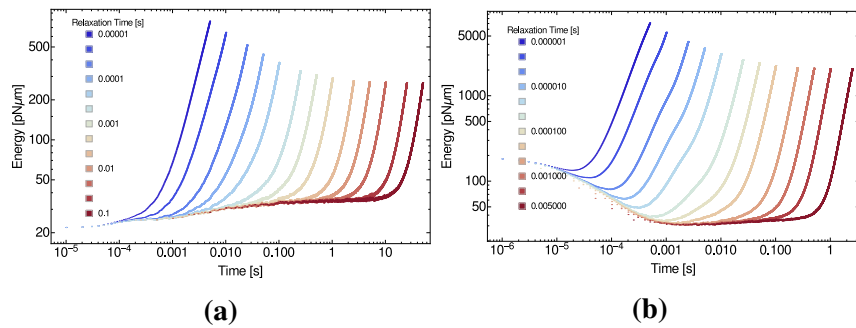


**Figure S2:** Strain energy as function of time for various relax times  $t_{relax}$  for networks with (a)  $k_{cl} = 10$  pN/μm and (b)  $k_{cl} = 100$  pN/μm crosslinked networks

## 6.4 Bundling

To contrast between bundling, contractility, and polarity sorting we computed the divergence of bundled networks, as well as the radial distribution function of the filament barbed ends in bundled networks. The results are shown in figure Figure S3.

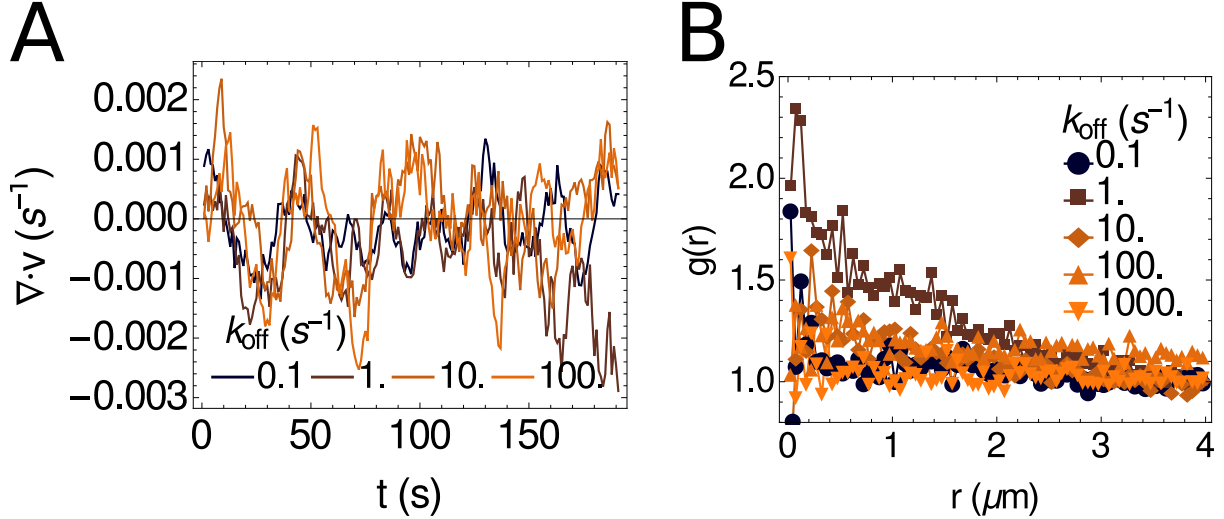


**Figure S3:** (A) Assemblies without motors that bundle do not show an average negative divergence, unlike assemblies with motors (Figure 6). (B) The radial distribution function for bundled networks for the barbed end of filaments is significantly less peaked than for all points on the filaments (Figure 2). Thus, the network is not polarity sorted.